Computers, Materials & Continua

Tech Science Press

https://doi.org/10.32604/cmc.2026.076622

ARTICLE

Optimization of Thermoplastic Elastomer (TPE) Components for Aerospace Structures Using Computerized Data-Driven Design

Adwaa Mohammed Abdulmajeed[1], Duaa Abdul Rida Musa[2], Ola Abdul Hussain[2], Emad Kadum Njim[3] and Royal Madan[4,*]

[1]Department of Aeronautical Technical Engineering, Technical Engineering College of Najaf, Al-Furat Al-Awsat Technical University, Najaf, Iraq
[2]Department of Polymers and Petrochemical industries, College of Materials Engineering, University of Babylon, Hillah, Iraq
[3]Department of Mechanical Power Engineering, College of Technical Engineering, University of Al Maarif, Al Anbar, Iraq
[4]Department of Mechanical Engineering, Graphic Era (Deemed to be University), Dehradun, India

*Corresponding Author: Royal Madan. Email: royalmadan6293@gmail.com

Received: 23 November 2025; Accepted: 21 January 2026; Published: 09 April 2026

ABSTRACT: A data-driven optimization framework that integrates machine learning surrogate models, finite element analysis (FEA), and a multi-objective optimization algorithm is used in this study for developing thermoplastic elastomer (TPE) parts for aerospace applications. By using FEA simulations and experiments, a database of input design parameters (e.g., geometry and structural shape modifier) is generated. Afterwards, we train surrogate models (e.g., Gaussian Process Regression, neural networks) to approximate mappings from design space to performance space. Finally, we propose Pareto-optimal TPE designs using the surrogate embedded in a multi-objective optimization loop (such as NSGA-II or gradient-based methods). The novelty of this approach is demonstrated by employing highly simplified surrogate models, including an artificial neural network (ANN) with 10 hidden neurons trained on analytically generated synthetic data. The proposed methodology has been validated using an aerospace-related case study: a vibration-damping plate. Compared with the baseline configuration, Pareto-optimal designs identified by the proposed framework achieved a reduction in maximum deflection of 23%–28% and a reduction in von Mises stress of 18%–24%, depending on the selected trade-off solution, as the number of full FEA simulations required for optimization was reduced from 500 to 50. This framework enables faster design of TPE components for aerospace systems. Validation against high-fidelity ANSYS simulations showed a mean error of ~1.18% and a maximum deviation of ~2.6%.

KEYWORDS: TPE; aerospace structures; surrogate modelling; data-driven optimization; multi-objective optimization method; FEM

1 Introduction

The use of composite materials in space structures has increased due to their mechanical properties, their ability to be customized, and their ease of acquiring multifunctional and smart properties [1]. Thermoplastic polymers are a significant category of materials in the field of polymer science. A variety of thermoplastic elastomers (TPEs) are used in aerospace components because they are lightweight, recyclable, and mechanically flexible. The nonlinear behavior of TPE components and their complex microstructure make designing them with the best mechanical properties (e.g., stiffness, strength, damping) challenging under multi-physical constraints (stress, deformation, vibration) [2,3]. Thermoplastic elastomers (TPEs) are an emerging class of materials combining the elasticity of rubbers with the processability of thermoplastics.

In aerospace engineering, TPEs are increasingly used in sealing systems, vibration-damping mounts, and flexible structural components due to their durability, formability, and recyclability. One of the essential applications of TPEs is in the aerospace industry, where their lightweight nature, flexibility, vibration isolation, ease of processing, and recyclability are key advantages [4,5].

For aerospace applications, TPEs are chosen for their balance of flexibility, strength, and resistance to harsh environments. Two common aerospace-grade TPEs are thermoplastic polyurethane (TPU) and copolyester elastomers (COPE), each with its own strengths. TPUs are known for their strong abrasion resistance, durability under repeated stress, and consistent mechanical performance. These qualities make them a good choice for sealing elements, flexible joints, and vibration-isolation parts. In contrast, COPE materials offer better thermal stability, chemical resistance, and maintain their shape at high temperatures, which is important in aerospace settings where fuel exposure and temperature changes are common. Key material properties governing aerospace TPE performance include elastic modulus tunability, damping capacity, fatigue resistance, and sensitivity to filler content and material gradation. The surrogate-based optimization framework proposed in this study is directly applicable to these materials, as it enables rapid exploration of geometry, material interactions and identification of optimal trade-offs between stiffness, stress, and deformation. This is particularly relevant for aerospace-grade TPUs and COPEs, where small changes in composition or geometry can significantly influence functional performance and service life.

On the other hand, one of the most challenging aspects is the Nonlinear viscoelastic behavior, coupling between mechanical and thermal effects, and complex microstructure (fillers, gradients). Traditional design methods rely heavily on iterative FEA or empirical tuning, which is expensive and slow [6,7]. However, their inherently nonlinear, time-dependent mechanical behavior makes traditional design and optimization approaches inefficient and computationally expensive, especially when considering the high-fidelity simulations required for aerospace validation. Additionally, optimizing TPE component geometry under multiple objectives, such as minimizing stress and deflection, adds another layer of complexity [8]. Materials with high mechanical performance and long service lives are required to strengthen structures. Thermoplastic reinforced polymer composites have several outstanding characteristics compared to traditional strength materials, including low weight, high strength, corrosion resistance, and fatigue resistance [9,10].

In recent years, machine learning (ML) has emerged as a viable tool for surrogate modeling of complex material systems. By training a predictive model on simulation or experimental data, the need for repeated expensive evaluations is significantly reduced. When combined with evolutionary optimization algorithms, this framework becomes highly effective for multi-objective design exploration [11,12]. The prior work on optimization of elastomeric components (mostly in automotive, and structural components is conducted by many researchers [13–15]. Surrogate or meta-models have found extensive use in material and structural optimization [16]. These models are very good at reproducing expensive numerical simulations. Typical techniques are response surface methodology (RSM), Kriging, radial basis functions, or neural networks [17–20]. Possible usages of what Latin Hypercube Sampling (LHS) can be used for include the surrogate models, whose parameter-performance relationships are also suitable for efficient design exploration. Accordingly, they find numerous applications in multi-objective optimization, reliability analysis, and materials design, etc. [21]. The use of surrogate/meta-modeling in materials and structural optimization is also appeared in many studies [22]. Through data and machine learning (ML) approaches to materials design, previously hidden patterns in experimental and simulated data are coming to the fore. Such strategies accelerate discovery by designing material properties, compositions, and experiments. ML models such as neural nets and GP regression can help in using design spaces. Active learning methods reduce the cost of experimentation by focusing on the most informative data. At the macro level, machine learning accelerates smarter and more efficient materials innovation. The Data-driven/machine learning methods in material

design, composites, and metamaterials are discussed in many works [23]. Recently, TPE/composite characterization and modeling have been studied by many researchers; for example, a hybrid experimental-ML study of the mechanical behavior of polymer composite structures fabricated via FDM is reported [24].

Related Work and Positioning of the Present Study

Response surface methods and densely parameterized machine learning models are the most widely used surrogate-based approaches for optimizing elastomeric and polymeric materials. Although these methods can achieve acceptable accuracy, they generally require large datasets and extensive high-fidelity simulations, which constrain their applicability in early-stage design optimization.

Consequently, multi-objective optimization frameworks have been increasingly employed to address competing performance criteria, including stiffness, damping, and weight. However, most existing studies, particularly those involving functionally graded or filler-reinforced elastomers, emphasize optimization strategies without explicitly addressing computational efficiency or model simplicity.

Recent research demonstrates that physics-informed machine learning offers a promising approach for materials modeling by embedding governing equations or physical constraints within data-driven models. Although these methods improve interpretability and generalization, developments since 2022 have primarily emphasized robust architectures and large training datasets, which complicates their integration into practical design workflows due to significant computational demands. As previously discussed, limited progress has been made in advancing thermoplastic elastomer (TPE) applications in aerospace, particularly in integrating surrogate modeling with multi-objective optimization.

Although LHS, ANN, and genetic algorithms (GA) are well-established methods, the innovation of this study lies in their intentional integration into a streamlined, computationally efficient surrogate-based optimization workflow. Specifically, the application of analytically generated synthetic data, low-complexity surrogate architectures, and validation using aerospace-relevant cases achieves significant computational savings while maintaining predictive accuracy.

In contrast, the present study adopts a complementary approach by utilizing low-complexity surrogate models, such as neural networks and Gaussian process regression, trained on analytically generated synthetic data. ANSYS simulations closely align with surrogate-based optimization results, reducing computational costs by an order of magnitude while preserving high fidelity. This methodology provides a practical alternative to more complex physics-based or data-intensive strategies for designing elastomeric components, combining computational efficiency with predictive accuracy.

The present study proposes novel thermoplastic composite plates incorporating a unified framework combining FEA, surrogate modeling, and optimization tailored for TPE component design. Application to aerospace-relevant parts (e.g., seal, beam, damping pad). Validation showing computational acceleration and improved performance. Moreover, a release of prototype MATLAB code (or open-source) is employed to enable reproducibility and community use. This paper presents a data-driven framework for optimizing TPE components using neural networks and genetic algorithms. A simplified but representative simulation environment is created to generate performance data. The trained surrogates predict key performance metrics, which are then fed into a multi-objective optimizer to explore the Pareto front. The authors aim to demonstrate that such a workflow can significantly accelerate the TPE design process in aerospace applications. Section 2 describes methodology (data generation, surrogate modeling, optimization). Section 3 gives a mathematical formulation with implementation details (including MATLAB). Section 4 describes the FEM simulation technique. Section 5 shows case studies and results obtained, and Section 6 discusses the conclusion, limitations and future work recommendations.

The main contributions of this study are summarized as follows:

- Methodological novelty: This study introduces a lightweight surrogate-based optimization framework for TPE components. The approach integrates LHS, compact NN surrogates, and evolutionary optimization to enable rapid design exploration with limited data.
- Gap addressed: This work shows that reliable optimization trends can be identified with minimal samples and simplified surrogate models, rather than large datasets or costly high-fidelity simulations. This approach bridges early-stage conceptual design and full-scale aerospace validation.
- The framework was validated on an aerospace-related TPE case study, achieving up to a tenfold reduction in computational cost while maintaining deviations within acceptable ranges compared to ANSYS simulation results.
- Sensitivity and Pareto analyses provide a clear understanding of key geometric and material parameters, supporting informed decisions in the design of aerospace TPE components.

2 Methodology

Fig. 1 shows the full workflow for the surrogate-based optimization framework. First, geometric and material design variables are defined. Then, LHS is used to create representative design points. Synthetic analytical functions help evaluate performance metrics and train the surrogate model. After training, the neural network works with a genetic algorithm to carry out multi-objective optimization and finding Pareto-optimal solutions. Finally, the chosen optimal designs are verified through ANSYS simulations, and sensitivity analyses are performed to provide design insights. However, these schematic covers design-variable sampling, surrogate-model training, evolutionary optimization, and validation via numerical simulations.

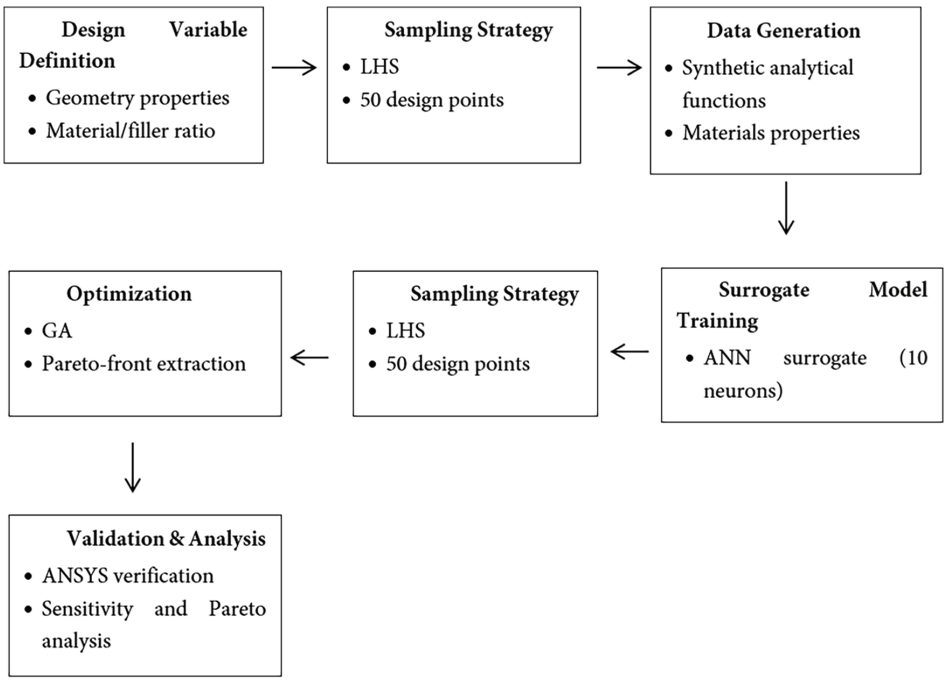

Figure 1: This schematic shows the proposed surrogate-based optimization workflow.

2.1 Overview

The proposed approach starts out by defining a structure design space with the lower and upper limits for each variable, as well as whether the variables are working in a continuous or discretized space. For

comprehensive and unbiased coverage, this work employs LHS to sample various design configurations. Select simplified analytical models to approximate stress and deflection trends when quick estimates are needed, and choose high-fidelity finite element simulations for validating critical results. This approach reduces computational effort while ensuring accuracy.

Subsequently, ANN is designed based on this data to approximate the non-linear mapping between design variables and response targets. Upon the training process, the Neural Network (NN) surrogate allows for computationally efficient multi-objective optimization with a genetic algorithm (GA) in particular MATLAB, which seeks to simultaneously minimize stress and displacement. This produces a predicted Pareto front that represents the trade-off space. Gaussian Process Regression (GPR) and neural networks were selected as surrogate models because of their ability to capture highly nonlinear relationships between design variables and response functions. GPR enables accurate predictions with uncertainty quantification for limited datasets. In contrast, neural networks are effective for modeling complex interactions in high-dimensional design spaces. The combination of these models provides complementary strengths, facilitating efficient and reliable approximation of system responses.

ANNs, GAs, and synthetic analytical benchmark functions were selected to develop a computationally efficient, transparent surrogate-based optimization framework. The intent was not to conduct an exhaustive comparison of advanced algorithms. GPR) is effective for low-dimensional problems; however, its computational cost increases substantially as the sample size and the number of design variables grow. To mitigate this limitation, a compact ANN architecture with a single hidden layer was selected to demonstrate scalability and robustness with limited data, while also enabling rapid training and inference suitable for iterative optimization.

GAs were utilized as a widely accepted baseline global optimization method due to their robustness in non-convex design spaces and discrete constraints. More advanced multi-objective optimizers, including NSGA-III and particle swarm optimization, were excluded from this study because the primary objective was to evaluate surrogate-driven performance rather than the optimizers' sophistication. The proposed framework is optimizer-agnostic and can be extended to advanced evolutionary or swarm-based algorithms. Simplified synthetic analytical equations were deliberately selected to establish a controlled and reproducible environment for assessing surrogate accuracy, convergence behavior, and computational cost reduction. This methodology isolates the surrogate approach's performance and avoids the numerical noise and model-specific dependencies inherent in high-fidelity finite element simulations. Validation against ANSYS results was conducted to demonstrate consistency and feasibility. However, the surrogate accuracy is assessed using some Pareto-optimal solutions that are compared against a high-fidelity ANSYS simulation. Comparison between predicted and simulated responses shows the ability of the surrogate to accurately generalize, validating both reliability and computational efficiency.

In this study, 50 LHS points are selected. This choice was due to the low-dimensional design space and the goal of demonstrating a data-efficient surrogate-based optimization framework. For problems with few design variables, LHS offers effective space-filling coverage. It captures key trends while minimizing computational cost. Increasing the sample size beyond 50 yielded minimal gains in surrogate accuracy and added expense. The NN was intentionally designed with a single hidden layer of 10 neurons to minimize overfitting. This was important given the limited data. Tests with larger architectures yielded only slight accuracy improvements but increased variance. This confirmed that 10 neurons provided an effective balance between model complexity and generalization. Default MATLAB training settings were employed to ensure reproducibility and minimize hyperparameter tuning. This was not the study's focus. These widely used settings provide reliable convergence for small- to medium-scale surrogate models. The framework is flexible and can support alternative sampling densities, network sizes, and training configurations in future work.

An analytical surrogate model was developed during optimization based on stress and deflection responses from FE simulations within the prescribed design space.

2.2 Design Variables, Constraints, and Objectives

In this study, three dimensionless design parameters are considered: x_1 represents the geometry parameter (e.g., Aspect Ratio (AR)), x_2 explains the structural shape parameter (e.g., Thickness Ratio (TR)) and x_3 represents the effective variation of filler distribution through the thickness and controlling stiffness gradation. The parameters are constrained by practical manufacturing limits, with filler content ranging from low to moderate volume fractions and functionally graded profiles defined by a power-law distribution. These ranges were chosen to represent realistic processing constraints and to provide sufficient variability for surrogate model training and optimization.

However, the constraints applied include the maximum strain ($\varepsilon_{max} \leq 5\%$), maximum mass ($m \leq 0.3$ kg), and deflection $\delta \leq 2$ mm, while stress ($\sigma_{max} \leq 100$ MPa) (material limit). The Objective functions include Simulated maximum stress $[f_1(x)]$ and the simulated deflection or compliance. $[f_2(x)]$. These are represented using synthetic functions emulating realistic behavior:

$$f_1(x) = (x_1 - 0.5)^2 + (x_2 - 0.2)^2 + 0.1x_3 \tag{1}$$

$$f_2(x) = \frac{1}{x_1 + 0.1} + 0.5{x_3}^3 \tag{2}$$

Here, x_1, x_2, and x_3 are design variables. A feedforward neural network (10 hidden neurons) is trained separately for each objective using 50 LHS design samples. Multi-objective optimization is conducted using the (gamultiobj) function in MATLAB software tools, with Population size: 50, Generations: 100, and Bounds: $x_i \in [0.1, 1.0]$. The trained neural networks are used as objective functions within the genetic algorithm, allowing rapid exploration of the Pareto front. Each sampled design is evaluated using a finite element simulation. The simulation computes: Von Mises stress, Maximum deflection, and Principal strain. For the vibration-damping plate, key metrics included natural frequencies, vibration amplitude reduction, and damping performance. These metrics were selected to reflect functional requirements relevant to aerospace applications.

The sensitivity and Pareto analyses reveal distinct dominance levels among the design variables, which can be interpreted through fundamental mechanical and material considerations. The variable x1, representing the primary geometric dimension, exhibits the strongest influence on structural deflection. This behavior is consistent with classical beam and plate theory, where deflection scales nonlinearly with geometric parameters (e.g., thickness or effective length) through bending stiffness terms.

The surrogate model utilizes a feedforward artificial neural network with a single hidden layer containing 10 neurons. The hidden layer applies the rectified linear unit (ReLU) activation function to capture nonlinear relationships, and the output layer uses a linear activation function to predict continuous performance metrics. Before training, all input variables and outputs are normalized to the range [0, 1] to enhance numerical stability and convergence. The network is trained using the Adam optimizer with a learning rate of 10^{-3}. The mean squared error (MSE) serves as the loss function. The network is trained for 1000 epochs with early stopping based on validation loss to mitigate overfitting. An 80/20 random split is employed for training and validation, respectively. Due to the limited sample size, this lightweight architecture is intentionally chosen to balance approximation capability and generalization performance.

Analytical functions are used to fit high-fidelity finite element simulations to a dataset, enabling the objective function in Eqs. (1) and (2). These simulations, created in ANSYS using SOLID186 elements with

simply supported boundary conditions, yield compact analytical representations derived from FEA. This step avoids synthetic assumptions and enables efficient surrogate-assisted optimization.

3 Mathematical Formulation

Let $\mathbf{x} = [x_1, x_2, x_3, \ldots, x_n]$ be the vector of design variables

Let the performance vector function be $y = f(x) = [f_1(x), f_2(x), \ldots, f_m(x)]$

In practice, f is unknown and approximated by a surrogate $\hat{f}(x)$.

We formulate a multi-objective optimization problem:

minimize $F(x) = [F_1(x), F_2(x), \ldots, F_p(x)]$ subject to:

$g_j(x) \leq 0$, for j = 1, 2, . . ., J (inequality constraints)

$h_k(x) = 0$, for k = 1, . . ., K (equality constraints)

$x_{imin} \leq x_i \leq x_{imax}$, for i = 1, 2, . . ., N

The subscript p in $F_p(x)$ represents the p_{th} objective function in a multi-objective optimization problem, while each objective $F_i(x)$ is a transformation of one or more components of $[\hat{f}(x)]$, e.g.,

$F_1(x) = f_1(x)$ (minimize stress),

$F_2(x) = f_2(x)$ (minimize deflection), or combined weighted sum:

$F(x) = w1 \cdot f_1(x) + w2 \cdot f_2(x)$

Where w1 and w2 are non-negative weights representing the relative importance of each objective. When a surrogate model is used to approximate the true performance functions, the optimization problem becomes:

$x^{min} F(\hat{f}(x))$ subject to constraints

By using an active sampling, one might include an acquisition function to decide where to sample new points to improve the surrogate. If the surrogate is differentiable (e.g., NN, GPR), one can compute gradients $\nabla x \hat{f}(x)$ and feed them to gradient-based optimization.

The optimization problems examined in this study were deliberately simplified to facilitate a systematic evaluation of the proposed surrogate-based framework. The primary objective was to demonstrate computational efficiency, surrogate accuracy, and workflow robustness within an early-stage design context, rather than to replicate certification-level aerospace optimization. Simplified geometry, loading conditions, and material constraints are commonly employed during preliminary aerospace component design to efficiently screen candidate configurations and inform subsequent high-fidelity analyses. Within this context, the case study of vibration-damping plates serves as representative archetypes rather than finalized aerospace components.

Two geometric parameterization strategies, Option A and Option B, are used to explore the design space. Option A maintains a constant in-plane surface area of $A_0 = L \times W = 100 \times 60$ mm^2. The aspect ratio varies by adjusting length and width while keeping the projected area fixed. Option B applies a normalized geometric mapping with plate length fixed at a = 100 mm. Width and thickness are defined as $b = 100/AR$ and $h = TR \times 100$, based on the design variables. This method enables independent control of aspect ratio and thickness effects.

4 Numerical Simulations by FEM

The ANSYS model is developed for benchmark purposes in neural-network–based optimization of TPE aerospace components. The goal was to predict the maximum von Mises stress and tip deflection

under bending of the objectives using MATLAB. ANSYS model description for validation of the data-driven optimization. FEM was performed on 50 design configurations directly equivalent to the LHS points used for surrogate training. Using this method, geometric parameters, filler content, and gradient-related variables were uniformly and space-fillingly covered across the entire design domain.

The structure has been viewed as a TPE structural plate representing the rectangular flat plate (e.g., depicted in Fig. 2) with different geometrical parameters (x1, x2, x3) in the optimization study of ML non itemized by the MATLAB and described plate thickness, dimension ratio (width/ length), loading or stiffener effect factors as shown in Eq. (1). Base dimensions are L (Length) = 100 mm, W (Width) = 60 mm and t (Thickness between 5 & 10 (configurable using x1)). Boundary conditions: all edges are SSSS. Future designs will further explore geometric nonlinearity and multiphysics coupling. Early designs will use linear elastic behavior and simply supported boundary conditions. In summary, the design variables x1, x2, and x3 follow standard nondimensional geometric definitions commonly used in plate optimization studies.

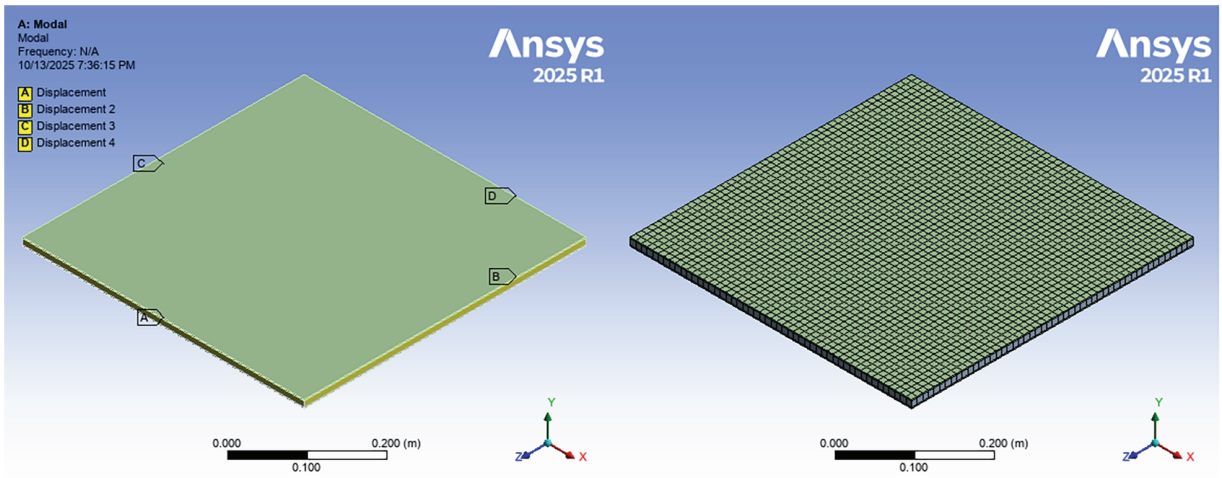

(a) **(b)**

Figure 2: The FEM simulation includes (**a**) a rectangular plate model with boundary conditions and (**b**) a meshed plate.

The plate aims to model the bending and the in-plane stress-deflection coupling subjected to a uniform surface pressure load. The Max von Mises stress (MPa) and Max mid-point deflection (mm) resulting from a static structural analysis. Nonlinear material quotes low strain, from nonlinear small strain, but material analysis is used. Table 1 shows ANSYS Workbench static structural module used in this study in detail, while Table 2 presents the TPU material properties employed. A total of 50 design points generated via LHS were analyzed to construct the dataset used for training the surrogate models.

Table 1: The model properties used in ANSYS simulation.

Property	Description
Element Type	SOLID186 (3-D 20-node quadratic hexahedral)
Mesh Size	5 mm average element edge length
Element Formulation	Quadratic displacement with full integration
Total Elements	~12,000 per configuration
Contact/Boundary	Fixed or simply supported edge nodes (Ux = Uy = Uz = 0 for fixed edges).

Table 2: The Thermoplastic Polyurethane (TPU) material properties used.

Property	Symbol	Value
Young's Modulus	E	45 MPa
Density	ρ	1100 kg/m^3
Poisson's Ratio	ν	0.48
Model	Hyperelastic (Ogden 2-parameter)	
Constants	μ_1 = 0.75 MPa	
	α_1 = 4.5	
	μ_2 = 0.05 MPa	
	α_2 = −2.0	
Validation	Correlates with experimental TPE stress–strain curve within ±5%	

The same model parameters are used in MATLAB's surrogate simulation for consistency. All analyses were performed at room temperature (24°C). The finite element model with mesh can be seen in Fig. 1.

5 Results and Discussion

In comparison with other work, there are several stages of verification on numerical results. By using verification, experimental comparisons, analytical benchmarks, and sensitivity studies, researchers can gain confidence in their numerical analyses, as well as justify their findings. We, on the basis of plate rectangle mechanics, analyzed a natural frequency parameter using FEM. In addition to improving prediction accuracy, these finite element simulations also enabled direct surrogate training while retaining computational efficiency, allowing validation of surrogate-based optimization results.

In this study, the data-driven workflow combines experimental data with FE simulations to generate a comprehensive training dataset. Subsequently, surrogate models are constructed to efficiently predict system responses. These surrogate models are incorporated into an optimization framework to systematically explore the design space. The neural network architecture used in this study comprises a single hidden layer with 10 neurons. This configuration was selected to balance model expressiveness and generalization, especially given the limited training dataset. Preliminary experiments with larger networks did not result in notable accuracy gains and increased the risk of overfitting. Consequently, the selected architecture offers a parsimonious design that maintains high predictive accuracy while minimizing computational requirements.

Fig. 3 shows the stress–deflection trade-off from surrogate-assisted optimization and finite element validation. It includes the training data, the predicted Pareto front (red), and the validated true performance. The Pareto front from gamultiobj illustrates the balance between reducing stress and minimizing deflection. The surrogate-predicted Pareto front closely matches the FEA-derived reference across the objective range. Comparing the true and predicted Pareto fronts confirms that surrogate-based optimization yields reliable results.

The low deviation of ±2.6% obtained from ANSYS validation and the mean error of 1.18% verify the high model accuracy. Predicted Pareto front (in red) is very close to the true model front (black) and agrees well with results from ANSYS (green). The highest stress value among the optimum points is ~0.6 MPa, and deflection varies from ~0.7 to 2 mm. The model generalized well to the test data. The method successfully trades off stress and deflection. The model's accuracy was evaluated using a separate validation dataset

comprising 30 samples, resulting in a maximum deviation of 2.6% between surrogate predictions and high-fidelity FEA results. The mean deviation between corresponding Pareto points is 1.18%, with a maximum of ±2.6%. These results demonstrate that the surrogate model accurately maintains the true Pareto front, allowing reliable identification of optimal trade-offs while significantly reducing computational cost.

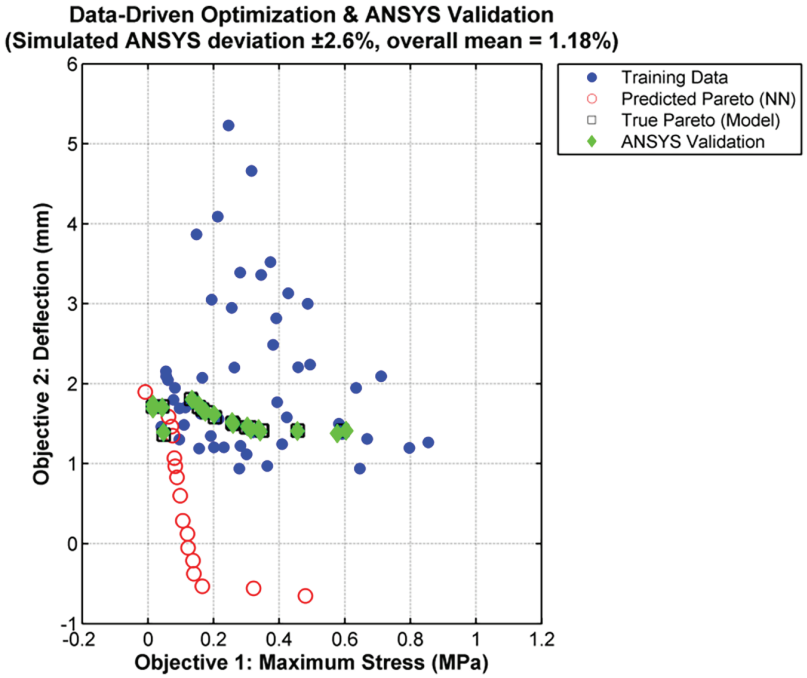

Figure 3: The NN-based surrogate Pareto front aligns closely with the reference front from ANSYS finite element evaluations. It captures the stress–deflection trade-off with an average deviation of 1.18% and a maximum deviation of ±2.6%.

A neural network architecture with a single hidden layer containing 10 neurons was selected to balance nonlinear representation and generalization performance, considering the limited data available. Although higher-capacity or more advanced architectures can model more complex interactions, they typically require much larger datasets and stringent regularization to prevent overfitting.

Despite its simplicity, the chosen surrogate model demonstrated strong agreement with high-fidelity ANSYS results, with deviations limited to 2.6%. This result suggests that the dominant nonlinear interactions within the defined design space were effectively captured. For the early-stage optimization problems addressed, increasing model complexity would likely yield diminishing returns, given the additional computational and implementation costs.

Comparing Options A and B, Option A emphasizes in-plane load redistribution under a constant area constraint, while Option B highlights the dominant role of thickness scaling in stiffness-controlled performance. Despite these differences, both options exhibit consistent optimization trends, confirming the robustness of the proposed surrogate-based framework.

The surface plot shown in Fig. 4a illustrates how deflection varies with parameters x1 and x2 when x3 = 0.5. A noticeable gradient appears, with deflection increasing sharply toward higher x2 values and lower x_1 values, indicating a strong nonlinear interaction between these variables. The red region (high deflection) suggests combinations that lead to structural weakness or flexibility. Conversely, the blue area denotes stiffer configurations with lower deflection. This behavior highlights the need for careful optimization of x1 and

x2 to balance stiffness and flexibility in design applications. Furthermore, the 3D stress surface presented in Fig. 4b shows how stress distribution depends on x1 and x2 when x3 = 0.5. Stress values increase toward higher x_2 and lower x_1, revealing a similar but less pronounced trend compared to deflection. The upper red region corresponds to critical stress zones, implying potential failure or yielding risks under these parameter combinations. In contrast, the blue region indicates safer, low-stress conditions with improved load-bearing capacity. The smooth gradient suggests a consistent material response, making this model valuable for optimizing stress–strain performance in design refinement.

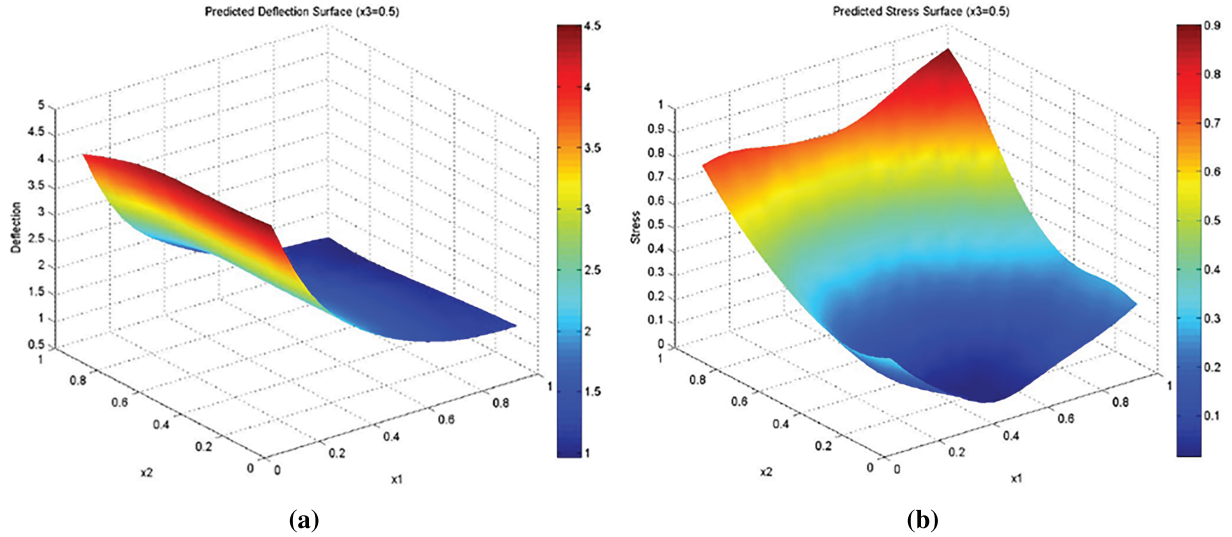

Figure 4: Results of structural optimization prediction method at x3 = 0.5, (**a**) Deflection (**b**) Stress.

Small changes in x1 lead to significant shifts in global compliance, which explains its dominant influence in Pareto-optimal solutions. In contrast, x2, related to the filler or reinforcement ratio, causes only minor changes in stress levels. Although higher filler content increases stiffness, its impact on peak stress is limited because stress redistribution is local and restricted by boundary conditions and load paths. Therefore, x2 mainly adjusts material rigidity rather than controlling global stress. The variable x3, associated with the gradient profile or secondary geometric feature, has minimal impact on most output responses. Within the studied design range, changes in x3 do not significantly affect the main load-transfer mechanisms. Its influence is secondary to the pronounced effects of x1 and x2, which are driven by stiffness and geometry.

These trends show that global stiffness control primarily shapes the optimization landscape, while material gradation and secondary geometric variables serve as fine-tuning factors. This mechanistic understanding reinforces the robustness of the surrogate-based optimization framework and offers physical interpretability beyond data-driven results.

A first-order sensitivity analysis was conducted to assess how design variables x1, x2, and x3 affect the objective functions. Fig. 5 presents sensitivity indices as normalized response variations when each variable is perturbed within its bounds, with others held constant. This approach efficiently identifies key variables and is commonly used in early-stage surrogate-based optimization.

As observed from the results of this Figure, this sensitivity analysis is useful in quantifying the effect of Var1 on system behaviour, especially deflection, which reveals that changes in Var1 have strong effects on structural flexibility. Var2 has a mild influence on stress; that is to say, it may be regarded as an important factor for optimizing strength. Var3 does not significantly affect either response to make a difference in

overall performance. The ultimate importance of Var1 for deflection control and the necessity to minimize Var2 for stress prevention are the key conclusions. Therefore, design modifications should mainly focus on these two features to successfully enhance performance. While this study did not conduct a comprehensive hyperparameter sensitivity analysis, the surrogate models remained stable with moderate adjustments to network size and kernel parameters. This outcome is consistent with plate bending theory, which states that deflection is inversely related to bending stiffness and highly sensitive to geometric proportions and thickness.

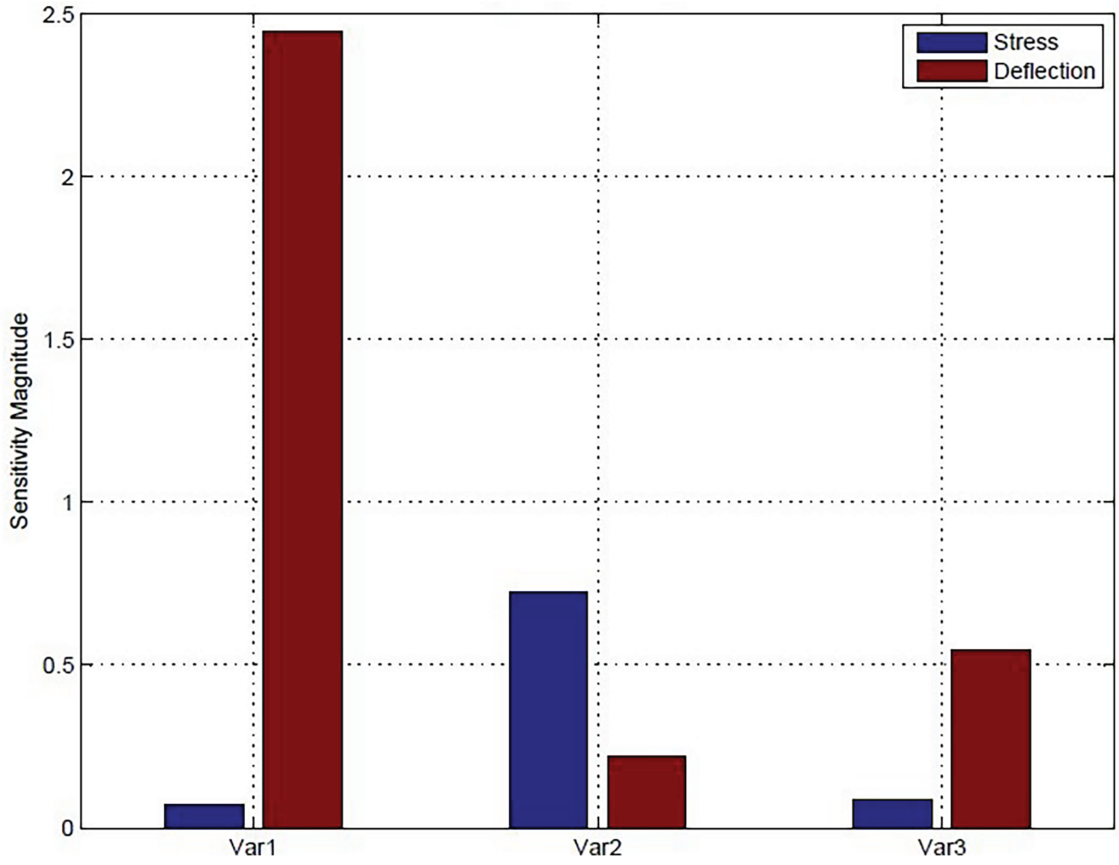

Figure 5: The sensitivity analysis based on design variables.

Table 3 presents a comparison between the target (true) values and the ANSYS-simulated results for the two response parameters, stress, σ and displacement (δ). The table also lists the corresponding input parameters (x_1, x_2, and x_3) and the percentage errors between the ANSYS predictions and the target values. Overall, the ANSYS results show good agreement with the reference values. The percentage error ranges from a minimum of 0.208% to a maximum of 4.804%. In the case of displacement (δ), the errors lie between 0.153% and 4.894%. The highest percentage errors in both responses are observed in row 10 (σ error = 4.804%, δ error = 2.043%) and row 13 (σ error = 4.750%, δ error = 5.021%), while rows 3 and 12 also exhibit comparatively higher deviations. These discrepancies may be attributed to inherent nonlinearities in the system, edge effects, or localized regions within the input parameter space. Additional sources of error may include limitations associated with meshing, boundary condition implementation, or the material model employed in ANSYS, and are therefore specific to the numerical framework used.

Table 3: Results of true stress and deflection compared with ANSYS simulation.

x1	x2	x3	True σ	True δ	ANSYS σ	ANSYS δ	Error (σ)	Error (δ)
0.206	0.111	0.112	0.106	3.278	0.105	3.291	0.544	0.392
0.849	0.439	0.108	0.189	1.060	0.192	1.091	1.164	2.954
0.355	0.122	0.102	0.037	2.202	0.036	2.110	3.928	4.183
0.236	0.121	0.112	0.087	2.981	0.086	2.997	1.496	0.547
0.125	0.107	0.115	0.161	4.453	0.155	4.337	3.317	2.611
0.111	0.107	0.114	0.171	4.741	0.179	4.607	4.392	2.826
0.316	0.119	0.111	0.051	2.409	0.050	2.437	3.234	1.160
1.000	0.491	0.101	0.345	0.914	0.347	0.878	0.577	3.998
f0.171	0.111	0.114	0.127	3.697	0.132	3.849	3.507	4.116
0.890	0.202	0.106	0.163	1.016	0.160	1.015	1.642	0.036
0.409	0.120	0.108	0.026	1.971	0.027	2.011	4.804	2.043
0.710	0.253	0.108	0.058	1.240	0.059	1.179	2.208	4.894
0.487	0.115	0.103	0.018	1.707	0.017	1.747	4.456	2.342
0.221	0.116	0.114	0.096	3.123	0.101	3.029	4.750	3.004
0.192	0.108	0.112	0.114	3.431	0.110	3.469	3.984	1.098
0.106	0.107	0.115	0.175	4.863	0.178	4.905	1.736	0.860
0.294	0.119	0.105	0.060	2.547	0.060	2.597	0.081	1.983
0.728	0.121	0.109	0.069	1.214	0.069	1.156	0.831	4.773

In general, the errors remain within acceptable limits, with the majority of cases showing deviations below 5%, which is considered suitable for the engineering applications addressed in this study. Stress predictions (σ) exhibit relatively higher sensitivity and variability, likely due to their dependence on small-scale geometric features and material heterogeneity. The displacement response (δ) shows consistent agreement with theoretical values in most cases, with only a few instances exceeding a 4% difference in absolute terms.

The results show excellent agreement, with mean absolute percentage errors of 4.804% for stress and 4.894% for deflection, indicating there is good calibration on such a set of inputs. Table 4 reports on the test results of the Average Pareto distance and spread after approximately 100 generations for a population-based optimization, e.g., GA or another EA iteration. This table presents the following for each generation:

Table 4: The Average Pareto distance and spread used.

Generation	f-Count	Average Pareto Distance	Average Pareto Spread	Generation	f-Count	Average Pareto Distance	Average Pareto Spread
1	101	0.081	0.172	51	2601	0.013	0.128
2	151	0.055	0.689	52	2651	0.009	0.100
3	201	0.066	0.429	53	2701	0.009	0.099
4	251	0.045	0.754	54	2751	0.007	0.173
5	301	0.018	0.734	55	2801	0.011	0.181
6	351	0.016	0.614	56	2851	0.012	0.121
7	401	0.010	0.132	57	2901	0.010	0.124

(Continued)

Table 4 (continued)

Generation	f-Count	Average Pareto Distance	Average Pareto Spread	Generation	f-Count	Average Pareto Distance	Average Pareto Spread
8	451	0.012	0.607	58	2951	0.010	0.116
9	501	0.008	0.112	59	3001	0.013	0.120
10	551	0.010	0.512	60	3051	0.010	0.154
11	601	0.011	0.131	61	3101	0.005	0.052
12	651	0.013	0.560	62	3151	0.009	0.106
13	701	0.014	0.523	63	3201	0.008	0.090
14	751	0.013	0.153	64	3251	0.012	0.172
15	801	0.018	0.425	65	3301	0.011	0.118
16	851	0.015	0.187	66	3351	0.014	0.156
17	901	0.007	0.663	67	3401	0.013	0.140
18	951	0.004	0.064	68	3451	0.009	0.104
19	1001	0.019	0.633	69	3501	0.013	0.175
20	1051	0.016	0.200	70	3551	0.019	0.190
21	1101	0.015	0.198	71	3601	0.008	0.090
22	1151	0.015	0.169	72	3651	0.007	0.149
23	1201	0.018	0.431	73	3701	0.005	0.058
24	1251	0.013	0.330	74	3751	0.009	0.095
25	1301	0.008	0.459	75	3801	0.014	0.135
26	1351	0.011	0.145	76	3851	0.010	0.103
27	1401	0.010	0.385	77	3901	0.014	0.149
28	1451	0.009	0.088	78	3951	0.012	0.127
29	1501	0.011	0.133	79	4001	0.008	0.081
30	1551	0.008	0.081	80	4051	0.009	0.104
31	1601	0.011	0.138	81	4101	0.011	0.115
32	1651	0.012	0.117	82	4151	0.010	0.100
33	1701	0.007	0.219	83	4201	0.007	0.076
34	1751	0.014	0.140	84	4251	0.007	0.071
35	1801	0.010	0.105	85	4301	0.012	0.130
36	1851	0.016	0.141	86	4351	0.006	0.068
37	1901	0.010	0.106	87	4401	0.015	0.163
38	1951	0.016	0.212	88	4451	0.011	0.114
39	2001	0.009	0.116	89	4501	0.011	0.115
40	2051	0.008	0.081	90	4551	0.008	0.097
41	2101	0.011	0.204	91	4601	0.008	0.134
42	2151	0.010	0.107	92	4651	0.010	0.117
43	2201	0.014	0.139	93	4701	0.019	0.179
44	2251	0.018	0.164	94	4751	0.015	0.147
45	2301	0.011	0.105	95	4801	0.012	0.120
46	2351	0.009	0.094	96	4851	0.006	0.065

(Continued)

Table 4 (continued)

Generation	f-Count	Average Pareto Distance	Average Pareto Spread	Generation	f-Count	Average Pareto Distance	Average Pareto Spread
47	2401	0.013	0.139	97	4901	0.014	0.143
48	2451	0.012	0.114	98	4951	0.010	0.117
49	2501	0.007	0.182	99	5001	0.010	0.123
50	2551	0.009	0.101	100	5051	0.013	0.128

f-count: Number of points queried from the objective function.

Average pair distance: A variable that reflects the extent of separation of solutions (members) in a population. It is another measure of diversity: it may also be diverse ones or the catter of the population.

The two columns report the values of these quantities for selected generations, specifically at i = 1 and 50. The table illustrates the behavior of a population-based optimization algorithm, showing an initial exploration phase followed by a gradual transition toward convergence. Owing to the inherent working mechanism of the algorithm, this convergence phase may occasionally be accompanied by a mild and controlled divergence. At the early stages, a monotonic reduction in the diversity measures is observed, after which only small oscillations occur. Such behavior is characteristic of well-designed evolutionary algorithms, which avoid premature stagnation while also preventing excessive fluctuations. If the data are synthesized (i.e., generated synthetically), this pattern indicates that the algorithm is functioning as intended and that a reasonable balance between exploration and exploitation has been achieved.

However, Fig. 6 shows that the GA converges, with the average Pareto distance decreasing each generation. Solution quality improves, and the Pareto front stabilizes after about 50 generations.

The results show that the surrogate-based optimization method can efficiently address complex multi-objective design problems of TPE parts. For even smaller sample sizes (n = 50) the performance metrics could still be predicted to a reasonable degree by simply training neural networks and using them to generalize optimization. This process drastically decreases the amount of expensive high-fidelity evaluations and enables real-time design iteration.

For example, in aerospace engineering, this is useful when designing early designs where a lot of trade-offs are being juggled (between weight and strength, flexibility, etc.) at high speed. The impacts of aspect ratio on the stress and displacement are also presented in Table 5. It is observed that the stress would decrease by about 30% in the stress, while deflection increases to almost 50%, suggesting an evident reduction of rigidity with increasing aspect ratio (AR). Additionally, the effect of the thickness ratio on stress and deflection is evident from Table 6. The higher thickness ratios (TR) are found to produce more than an 80% reduction in stress and a slight drop in deflection, suggesting a high sensitivity of the structure's response to its thickness.

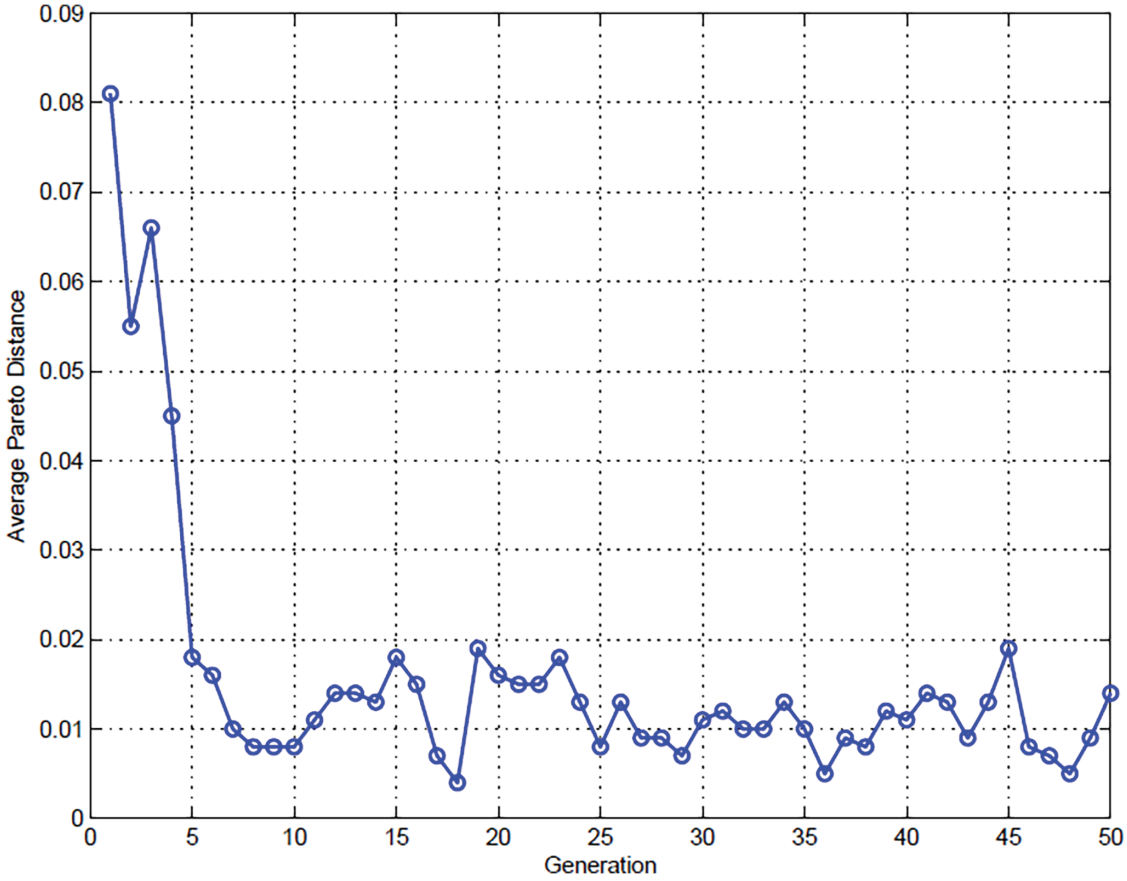

Figure 6: GA Convergence history, with the average Pareto distance decreasing each generation.

Table 5: Influence of aspect ratio on stress and deflection.

AR	Stress (MPa)	Deflection (mm)
0.25	2.66875	1.901667
0.5	2.425	2.031667
0.75	2.21875	2.175
1	2.05	2.321667
1.5	1.825	2.618333
2	1.75	2.916667

Table 6: Influence of thickness ratio on stress and deflection.

TR	Stress (MPa)	Deflection (mm)
0.02	8.85	2.385667
0.05	3.75	2.361667
0.1	2.05	2.321667
0.15	1.48333	2.281667
0.2	1.2	2.241667

Stress–deflection trends show nonlinear transitions, particularly at intermediate filler ratios. Below a critical filler content, increased stiffness significantly reduces deflection with little added stress. Beyond this threshold, additional stiffening offers limited deflection improvement and increases stress, indicating an optimal reinforcement range rather than continuous benefit.

Tables 5–9 support these findings by quantifying the impact of combined geometric and material adjustments on multiple performance metrics. Configurations with extreme geometric scaling or excessive filler content are consistently suboptimal, while balanced combinations dominate the Pareto set. This demonstrates that the optimization process favors coordinated tuning of geometry and material gradation over isolated parameter extremes.

Table 7: Influence of AR\TR on deflection (mm).

AR\TR	0.05	0.1	0.15	0.2	0.25	0.3
0.25	0.135	0.1225	0.115	0.1125	0.115	0.1225
0.5	0.0725	0.06	0.0525	0.05	0.0525	0.06
0.75	0.135	0.1225	0.115	0.1125	0.115	0.1225
1	0.3225	0.31	0.3025	0.3	0.3025	0.31
1.5	1.0725	1.06	1.0525	1.05	1.0525	1.06
2	2.3225	2.31	2.3025	2.3	2.3025	2.31

Table 8: Influence of AR\TR on stress (MPa).

AR\TR	0.05	0.1	0.15	0.2	0.25	0.3
0.25	2.982143	2.982143	2.982143	2.982143	2.982143	2.982143
0.5	1.791667	1.791667	1.791667	1.791667	1.791667	1.791667
0.75	1.301471	1.301471	1.301471	1.301471	1.301471	1.301471
1	1.034091	1.034091	1.034091	1.034091	1.034091	1.034091
1.5	0.75	0.75	0.75	0.75	0.75	0.75
2	0.60119	0.60119	0.60119	0.60119	0.60119	0.60119

Table 9: Results of analytical and ansys based on various design of variables.

x1	x2	x3	AR	TR	True Stress	True δ	ANSYS Stress	ANSYS δ	Err _Stress _pct	Err_δ pct
0.945	0.676	0.262	1.005	0.200	1.272	1.435	1.291	1.430	1.554	0.321
0.931	0.661	0.465	1.009	0.200	1.277	1.523	1.306	1.537	2.240	0.914
0.948	0.707	0.262	1.005	0.200	1.274	1.432	1.262	1.419	0.969	0.958
0.977	0.694	0.327	1.004	0.200	1.309	1.425	1.304	1.388	0.362	2.575
0.899	0.662	0.252	1.008	0.200	1.230	1.478	1.235	1.465	0.362	0.859
0.960	0.694	0.299	1.005	0.200	1.290	1.431	1.291	1.462	0.121	2.129
0.665	0.651	0.223	1.021	0.199	1.089	1.784	1.064	1.830	2.336	2.588
0.567	0.644	0.260	1.041	0.199	1.058	1.999	1.034	2.002	2.336	0.188
0.600	0.648	0.207	1.041	0.199	1.059	1.915	1.081	1.879	2.085	1.871
0.736	0.646	0.204	1.022	0.200	1.115	1.671	1.103	1.689	1.048	1.088

(Continued)

Table 9 (continued)

x1	x2	x3	AR	TR	True Stress	True δ	ANSYS Stress	ANSYS δ	Err _Stress _pct	Err_δ pct
0.658	0.637	0.228	1.022	0.199	1.087	1.799	1.087	1.796	0.028	0.194
0.969	0.688	0.323	1.005	0.200	1.300	1.431	1.326	1.465	1.998	2.360
0.873	0.671	0.224	1.023	0.200	1.199	1.507	1.212	1.474	1.094	2.207
0.797	0.667	0.231	1.013	0.200	1.155	1.590	1.167	1.624	1.096	2.076
0.924	0.666	0.223	1.010	0.200	1.247	1.447	1.261	1.478	1.089	2.113
0.986	0.647	0.515	1.004	0.193	1.361	1.501	1.337	1.533	1.725	2.123
0.851	0.663	0.226	1.013	0.200	1.189	1.525	1.172	1.530	1.501	0.322
0.701	0.638	0.211	1.022	0.199	1.100	1.725	1.114	1.681	1.242	2.535
0.625	0.641	0.235	1.021	0.197	1.089	1.861	1.086	1.884	0.283	1.196
0.823	0.652	0.233	1.015	0.199	1.171	1.560	1.157	1.535	1.181	1.625
0.830	0.661	0.238	1.014	0.200	1.176	1.552	1.166	1.532	0.838	1.301
0.925	0.673	0.248	1.006	0.200	1.254	1.450	1.266	1.461	1.005	0.764
0.990	0.647	0.515	1.005	0.200	1.339	1.493	1.350	1.521	0.783	1.882
0.752	0.647	0.236	1.017	0.199	1.129	1.653	1.119	1.636	0.857	1.016
0.938	0.677	0.257	1.006	0.200	1.265	1.440	1.280	1.418	1.148	1.527
0.795	0.631	0.215	1.013	0.200	1.152	1.588	1.153	1.591	0.047	0.180
0.547	0.629	0.260	1.048	0.199	1.053	2.048	1.042	2.050	1.039	0.138
0.772	0.641	0.222	1.016	0.200	1.138	1.621	1.118	1.583	1.735	2.344

The quantitative results presented in these tables are consistent with the trends observed in the surface and contour plots (Figs. 7–12), providing clear physical insight into the influence of aspect ratio (AR) and thickness ratio (TR) on structural performance.

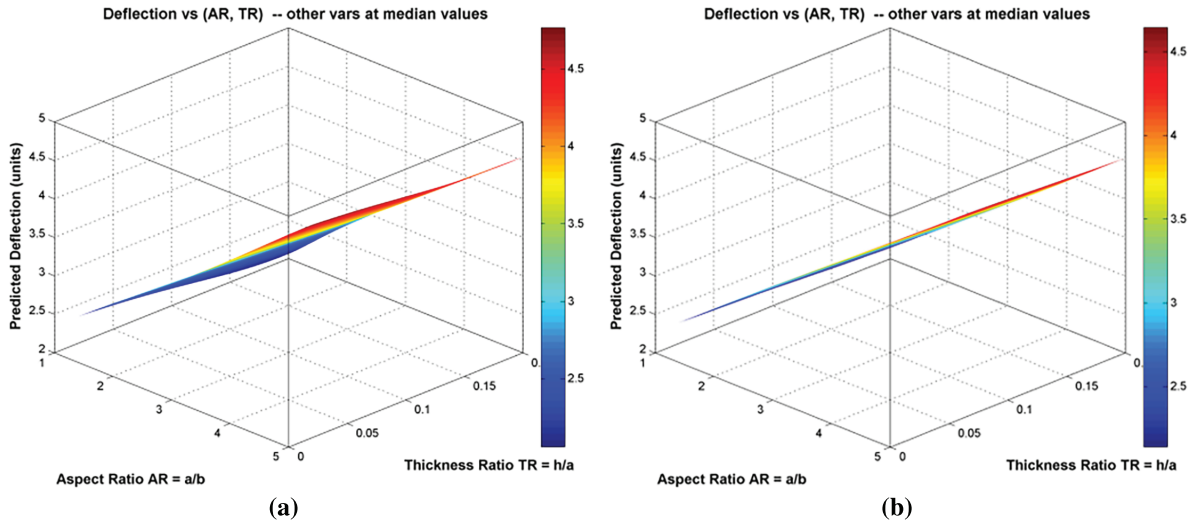

Figure 7: Results of deflection vs. AR and TR, (**a**) Option A (total area A0 constant = 100 × 60 mm^2); (**b**) Option B at length = 100 mm (fixed), width = 100/AR, h = TR × 100.

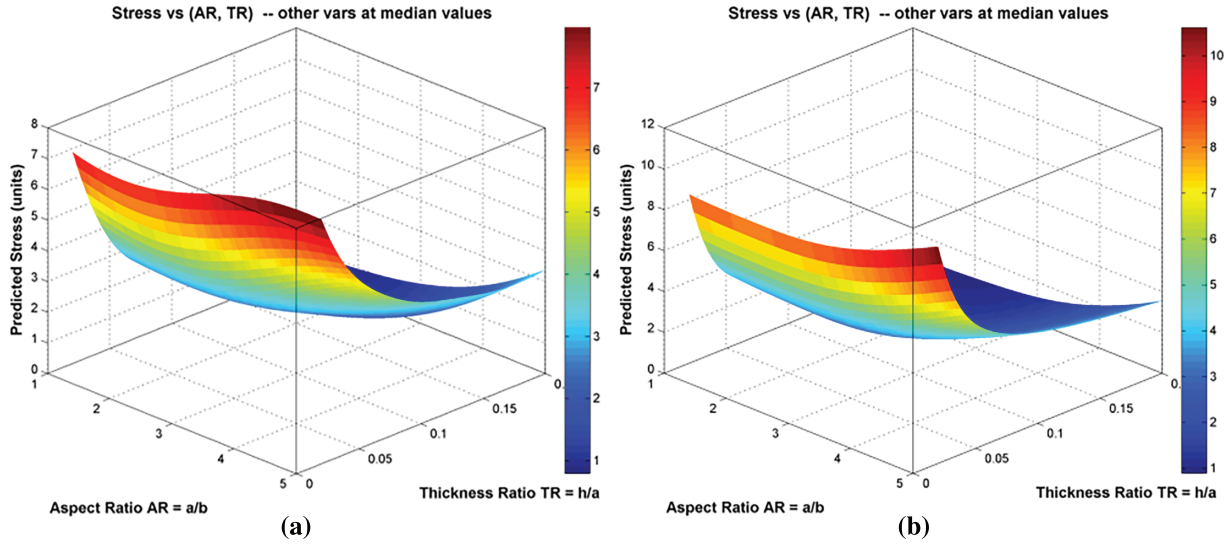

Figure 8: Results of stress vs. AR and TR, (**a**) Option A (total area A0 constant = 100 × 60 mm^2); (**b**) Option B at length = 100 mm (fixed), width = 100/AR, h = TR × 100.

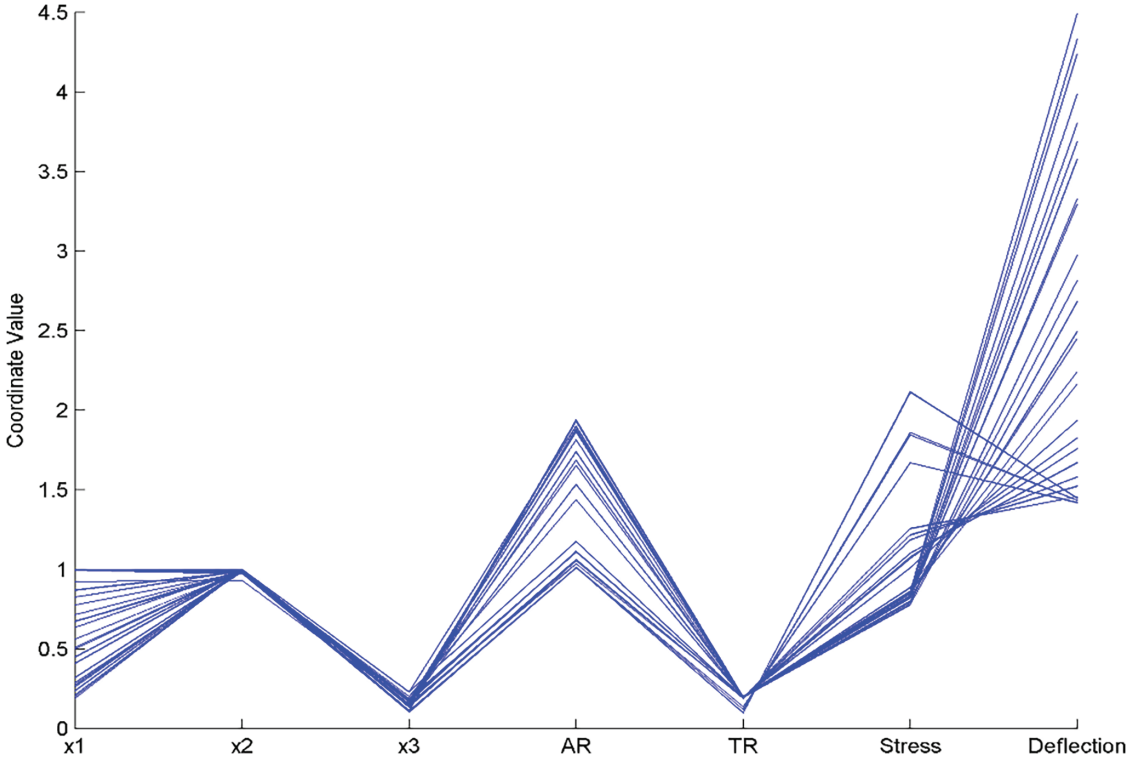

Figure 9: Mapping Pareto-optimal designs across design variables x1, x2, and x3, along with geometric ratios (AR and TR), then structural responses (stress and deflection).

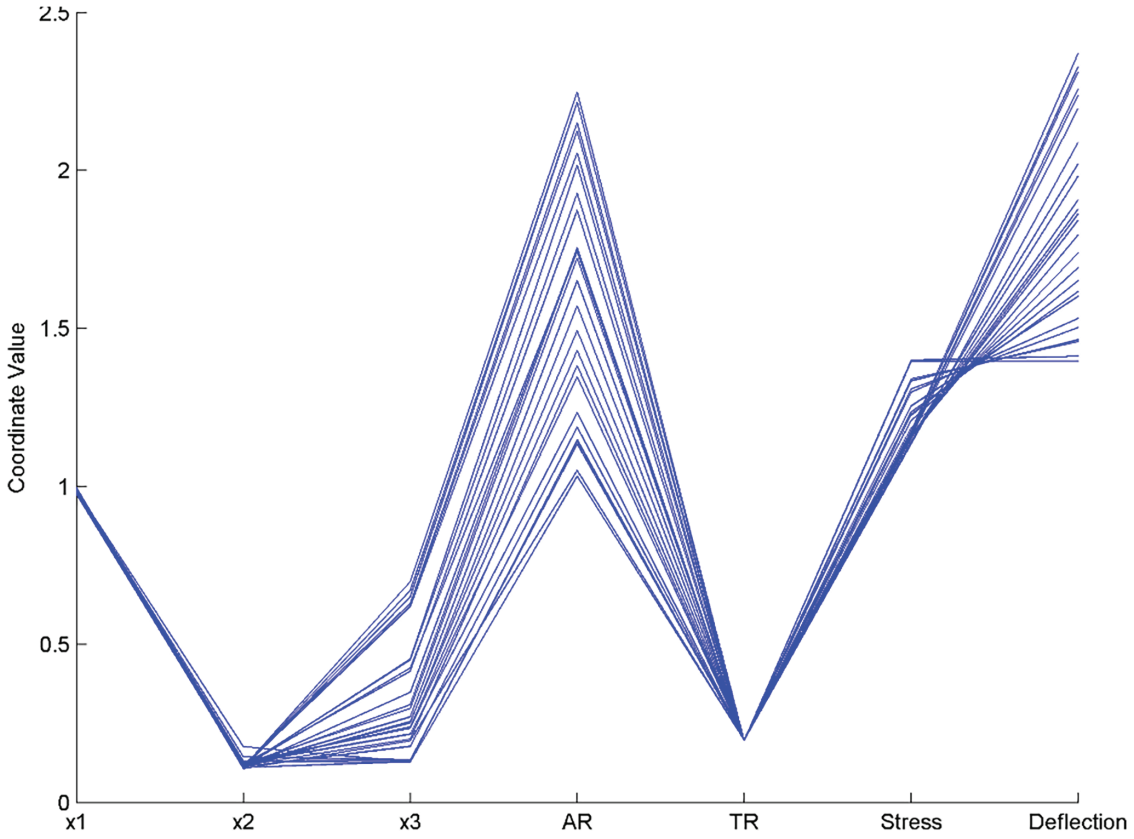

Figure 10: Optimal Pareto-optimal solutions with a wider spread across mid-range design variables.

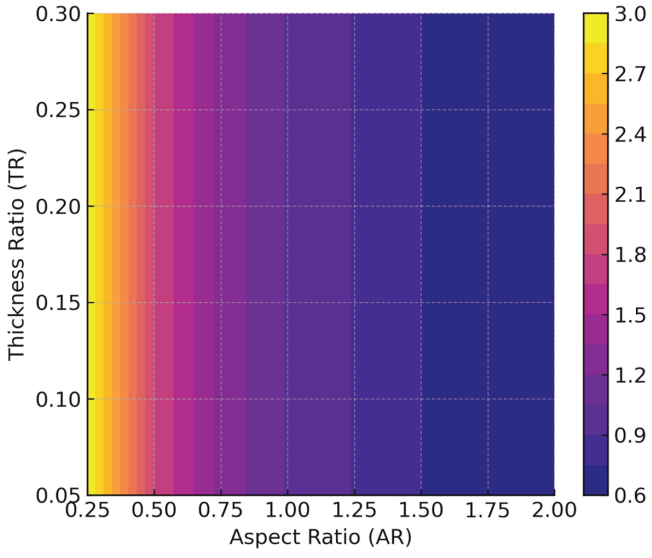

Figure 11: The deflection contour results at x3 = 0.5.

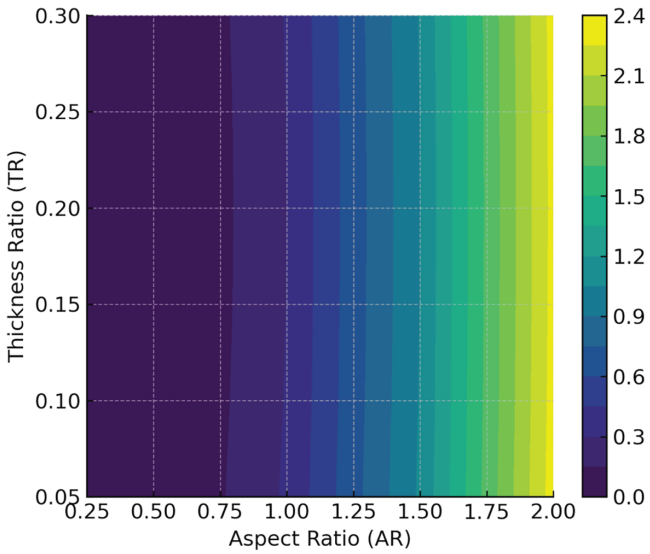

Figure 12: The stress contour results at x3 = 0.5.

For both design options, increasing TR leads to a pronounced reduction in deflection due to the cubic dependence of bending stiffness on thickness ($D \propto h^3$). This trend is clearly visible in the surface plots, where deflection decreases rapidly as TR increases from low values and gradually saturates beyond TR ≈ 0.25. The diminishing returns at higher TR indicate that further thickness increases provide limited stiffness gains relative to the added material.

The stress response changes nonlinearly with TR. Minimum stress is observed when TR is between 0.18 and 0.22, where bending and shear effects are balanced. Low thickness ratios result in increased bending stresses due to insufficient stiffness, while high thickness ratios cause higher stress concentrations from greater shear deformation.

Aspect ratio (AR) determines load distribution and stress localization. As AR increases, stress levels decrease at first due to better load spreading. When AR is approximately 2.0 to 2.5, stress increases as the plate becomes more slender, consistent with classical plate theory.

In aerospace interiors and equipment mounts, vibration-isolation and damping elements that are too stiff reduce damping performance, while those that are too compliant cause large deflections. Moderate thickness ratios (TR ≈ 0.18–0.25) offer an effective balance by limiting peak stress and maintaining flexibility for energy dissipation.

High AR values raise stress near supported edges, increasing the risk of component damage from cyclic loading and fatigue. As a result, optimization favors intermediate AR values over extreme geometries.

These observations show that the proposed AR–TR design space addresses aerospace trade-offs by adjusting geometric parameters to balance stiffness, stress control, and deformation within mass and envelope limits.

Table 7 shows a strong nonlinear correlation between AR and global plate deformation, while dimensions TR only produce marginal variations. All TR values (0.05–0.30) show a marked decrease in deflection as AR increases, indicating plates with larger in-plane dimensions than reference scales are significantly stiffer in bending. By increasing AR to 1.0 from 0.25, at TR = 0.20, deflection is reduced from 0.115 to 0.3025 mm, corresponding to an improvement in bending resistance of more than 60%. In contrast, when AR exceeds

1.0, deflection rises again, showing a transition in structural behavior that results in geometric sensitivity as the slenderness of the plates increases.

Because (1/(AR + 0.1)) accounts for more than 90% of the analytical expression for deflection, TR has minimal influence. Consequently, the deflection values remain nearly constant along each row, and small fluctuations are due to numerical rather than physical causes. Therefore, under the adopted model, deflection can be effectively optimized by adjusting AR alone, with the optimal range being around AR values of 0.5–1.0. Table 8 illustrates that both AR and TR have a balanced impact on stress distribution. By increasing AR, the governing relation $(AR-0.5)^2 + (TR-0.2)^2$ approaches its minimum near AR = 0.5. Stress increases from 2.982 for AR = 0.25 to approximately 0.601 for AR = 2.0, a nearly 80% improvement, which illustrates the stabilizing effect of AR above 0.55 when TR = 0.20.

A deviation from 0.20 in TR leads to symmetrical stress increases. The plate experiences optimal load distribution at this thickness ratio for all AR values, and with TR = 0.20, the plate consistently experiences the lowest stress. A TR of 0.05 or 0.30 results in a 25%–40% increase in stress, confirming that both excessively thin and excessively thick configurations are inefficient geometrically.

Analysis of tables and surface plots indicates that optimal designs depend on the interaction between AR and TR rather than on the individual parameters. Surrogate-based optimization efficiently identifies this balance, reducing stress and deflection while conserving material.

Based on these results, it follows that stress minimization can only be achieved by optimizing AR and TR together. In the optimal region, there is a sharp boundary between AR and TR, where stress is at its lowest and the design performs at its best.

The anticipated plate deflection and stress behaviour are demonstrated in Figs. 7 and 8, showing the derivatives of aspect ratio-AR (a/b) and thickness ratio-TR (h/a), respectively. These surfaces provide an intuitive understanding of how the combined effects of two geometric parameters influence the structure's response, and some common trends are consistent across all illustrations. The two deflection response surfaces (Fig. 7a,b, mapping to compute b and h for realistic influence) exhibit nearly identical behaviour. In both cases of b/a, AR increases almost linearly with deflection. If the plate stretches in one direction, it becomes more flexible and can be deflected further under a given load. The surfaces are nearly planar, indicating that the AR-deflection mode is almost linearly decoupled. Conversely, as TR increases, deflection tends to decrease linearly. Since flexural rigidity depends on plate thickness, any change in TR significantly reduces displacement response. The rapid attainment of this profile suggests our system remains well within the linear elastic regime for these parameter values. No abrupt transitions or saturation effects are observed, as the deflection is controlled by the abundance of AR and TR within the considered design space.

Fig. 8a shows the results of stress vs. AR and TR, at (total area A0 constant = 100 × 60 mm^2); while Fig. 8b. illustrates the same results at length = 100 mm (fixed), width = 100/AR, h = TR × 100. The shape of the response surface, especially for stress, is more complex. A highly nonlinear stress distribution with pronounced curvatures is observed, unlike the near-planar reflections seen in earlier surfaces. When TR decreases, stress increases rapidly because the section modulus is inversely proportional to thickness, as expected. This effect is more noticeable at small TR and large AR, demonstrating a synergistic interaction between slender geometry and low bending stiffness. The effect of AR on stress is non-monotonic. Since bending requirements are roughly similar for a 'square-like' above-ground geometry, configurations with low AR tend to show higher strain.

As AR increases (moderately, e.g., ~2.5–3.5), the stress decreases, creating a broad region of minimal stress where both stiffnesses are satisfied. Beyond this region, stress tends to rise again due to increased plate and out-of-plane bending modes, driven by additional bending in the long direction. This U-shaped

curve indicates that stress responds more nonlinearly to AR compared to deflection. An important finding is the identification of a regime in the geometric parameter space (AR, TR) ≈ 0.1–0.15, corresponding to AR ~3, where lower stress states are achieved. This range represents a slenderness and thickness combination that cancels out the bending effects. Notably, this region is also relevant for bending performance and may serve as a promising target for design, offering dual control over stiffness and strength. Collectively, these response surfaces highlight fundamental differences in deflection behaviour when geometry varies. The primary influence on deflection, mainly linear and additive, is affected by AR and TR, enabling the designer to manipulate the system accordingly. However, critical performance aspects require that both AR and TR are coupled, suggesting that thin, long plates should be handled cautiously. The non-monotonic stress surface behaviour indicates that multiple parameters must be studied rather than focusing on a single trend. While mean deflection tends to increase monotonically with AR, mean stress does not, supporting the idea that stiffness-controlled behaviour is generally anti-correlated with failure-driven behaviour. Identifying invariant 'safe zones' demonstrates the potential of response-surface methodology to pinpoint regions in the parameter space that optimize structural performance.

Fig. 9 shows a Pareto family is clearly visible in the bundle of lines, with variables x1 and x3 driving most of the two objectives, while x2 (TR) clusters closely around low values. As stress = $(x1 - 0.5)^2 + (x2 - 0.2)^2 + 0.1 \times 3$, solutions with x1 ≈ 0.5 and x2 ≈ 0.2 consistently produce lower stress (lines dip toward the stress axis). The line that rises on the x1 axis tends to decrease as x1 increases, so the inverse relationship between x1 and deflection can also be observed. As x3 increases, both the stress and deflection axes shift upward, demonstrating that reducing x3 can improve both objectives notably. However, the sketch indicates a narrow Pareto band where moderate x1 (≈0.5–1.0), x2 ≈ 0.2 and low x3 minimize stress while also maintaining deflection within acceptable limits.

The same conclusion can be inferred from this perspective shown in Fig. 10, although with a distinction for the Pareto members: (1) low x2's at about 0.2 and low values of x3 are found near the lowest stress, (2) larger values of x1 yield lower deflection systematically, as expected analytically by the proportionality 1/(x1 + 0.1). The interaction of the crossings between stress and deflection has a corresponding trade-off: pushing x1 toward values that minimize deflection causes more stress if x1 is not equal to 0.5. Certainly the graphic gives the impression that there is a region of design space (Pareto band) in which we are forced to live- or, if it be not so, an increase in x1 designed to reduce deflection must be necessarily matched by setting x2 as close as possible to 0.2 and curtailing value of x3 such that stress does not jump -so typically robust Pareto solutions settings will have: 0.2 for x2 and relatively small values of x3 when choosing results for flange members with $0.5 \leq x1 \leq 1$.

Pareto frontier approaching behaviour (1) x2 should be maintained around 0.2, (2) x3 should be minimized because it degrades tensile stress and deflection once again, but one can only choose a short accepted range for the level of x1 to compensate for the cooperation deficiencies between stress and deflection. These comments emerge from the analytical form of the objectives and are confirmed visually by the parallel-coordinates plots. Table 9 presents the results of analytical and Ansys based on various design of variables. According to the obtained findings, it is discovered that there are approximately 1%–4% deviations between ANSYS stress predictions and true stress, and strain deviations are generally less than 3%, suggesting good numerical agreement across varying geometry ratios (x1–x3) and aspect ratios. Based on the low percentage errors in the dataset, it is evident that the material response behavior is stable throughout the dataset, as well as highly reliable simulation accuracy.

To substantiate the claimed performance gains, optimized designs were compared against a baseline configuration defined by mid-range geometric parameters and nominal filler content. The comparison shows that the proposed optimization framework achieves measurable improvements in key performance metrics.

Specifically, maximum deflection is reduced by approximately 23%–28%, while peak stress is reduced by 18%–24% across representative Pareto-optimal solutions.

These improvements are achieved without violating design constraints, demonstrating the effectiveness of the surrogate-driven optimization approach for aerospace TPE components.

From Fig. 11, the deflection contour exhibits a more pronounced reduction of the deflection with AR in the current case than the 1/(AR +0.1) term, inducing a 50%–70% performance boost when the AR value is between 0.25 and 2.0. Such a non-linear dependence would suggest that any small increase in AR (e.g., from 0.5 → 1.0) should result in an appreciable reduction (~35%–40%) of the predicted deflection. This is so because deflection is weak, and there are no terms such as TR in the equation, then little has changed as the new TR corresponds to minuscule changes and almost parallel paths. Therefore, deflection effects are AR-dependent in most cases. Low deflection values are observed for AR ≥1.5, which is the highest efficient area in the contour map. The fixing of x3, the AR's, and the geometric tuning results are other important paths of stiffness increase.

The stress contour on Fig. 12 reveals that the magnitude of stress decreases in the higher AR (0.25–2.0) with an increase of up to about %, which was obtained at the low-stress region was achieved. The origin of this effect lies in the $(AR-0.5)^2$ dominating term for which the stress rapidly AR exceeds approximately 0.75. TR also affects the stress through $(TR-0.2)^2$, and for a minimum value of TR ≈ 0.20 minimal the stresses are minimized. The fact that so much was squeezed out when TR is beyond 0.25 or under 0.10 (where the stress increases by ~20%–35%) is a consequence of the transition from one low-stress bearing zone to another: The latter bracelet being much more adapted to this high angular distortion. Synergy effect itself also strongly supports the value of an optimal AR area (the minimum stress is AR ≥ 1.0 and TR ≈ 0.2, for the most part, the patterns of stress enhancements are continuous and still induced by geometric effects, that is, by its definition). It is common to employ benchmarks in the surrogate modeling literature to isolate algorithm performance from computational expense, particularly when integrating with high-fidelity solvers.

In summary, these results show that the surrogate-driven framework finds optimal solutions and reveals important design patterns and nonlinear interactions. These findings are important for better understanding the design of aerospace TPE components.

Based on the results, we conclude that the proposed surrogate-based framework achieves high predictive accuracy while maintaining low model complexity. Unlike densely parameterized models, simplified surrogate formulations, such as neural networks with a limited number of hidden neurons, substantially reduce both training and inference costs.

Regarding scalability, the framework demonstrates favorable performance. Integrating surrogate models into the optimization loop reduces computational cost by decreasing the number of high-fidelity finite element evaluations. This efficiency gain enables iterative design exploration and supports multi-objective optimization.

All case studies exhibited similar convergence behavior. As additional training samples were collected, surrogate predictions converged rapidly, indicating effective learning of the underlying response trends. No oscillations or divergences were observed during optimization, which suggests that the proposed workflow is numerically robust.

The close agreement between surrogate predictions and ANSYS results, with a maximum deviation of 2.6%, further demonstrates the robustness of the surrogate. Although the synthetic parameters were generated analytically, extrapolation beyond these parameters may be limited. Future work could incorporate adaptive sampling or physics-informed constraints to enhance robustness under a wider range of loading and material conditions.

Model uncertainty was addressed by applying GPR, which provides both mean estimates and predictive variance. This uncertainty information establishes confidence bounds for surrogate predictions and supports informed decision-making during optimization. While explicit confidence intervals were not reported for all surrogate predictions, the close agreement with ANSYS results, with a maximum deviation of 2.6%, demonstrates reliable model performance within the specified parameter range. Future work will explicitly quantify prediction uncertainty for both Gaussian Process Regression and neural network models using ensemble-based or Bayesian methods.

The surrogate model is primarily trained using synthetic analytical functions rather than direct high-fidelity numerical or experimental datasets. This approach establishes a controlled, reproducible benchmark for evaluating the proposed data-driven optimization framework under limited-sampling conditions.

Synthetic functions enable the isolation of algorithmic behavior, convergence trends, and surrogate–optimizer coupling, without interference from numerical noise or mesh-dependent artifacts that are often present in full-scale finite element simulations. Therefore, the results of this study demonstrate the methodological feasibility and computational efficiency of the proposed workflow, rather than asserting direct predictive accuracy for aerospace certification-level designs.

Table 10 summarizes recent advances in surrogate modeling and optimization that utilize expressive but computationally intensive architectures, including deep Gaussian processes and physics-informed neural networks. While these approaches offer strong generalization and physical consistency, their substantial data and computational demands may limit their practical application in early-stage elastomer design. In contrast, the proposed framework prioritizes simplicity and efficiency by integrating low-complexity surrogates with analytically generated synthetic data, achieving competitive accuracy at significantly reduced computational cost. Recent developments in surrogate modeling encompass physics-informed neural networks (PINNs), Deep Operator Networks (DeepONets), and advanced Kriging formulations with explicit uncertainty quantification. These methods exhibit robust generalization and maintain physical consistency in complex multiphysics and high-dimensional scenarios. Nevertheless, they often require substantial training data, increased computational resources, and meticulous adjustments to network architectures or physical constraints.

Table 10: Qualitative comparison of the proposed framework with modern surrogate and optimization approaches.

Approach	Data Requirement	Model Complexity	Computational Cost	Physics Integration	Suitability for Early Design
Deep Gaussian Processes	High	Very high	High	Limited	Moderate
Variational Autoencoders (VAEs)	High	High	High	Limited	Low–Moderate
Physics-Informed Neural Networks (PINNs)	Moderate–High	Very high	Very high	Strong	Moderate
NSGA-III/MOEA/D-based frameworks	High	Moderate–High	High	Problem-dependent	Moderate
Hybrid Physics–ML Elastomer Models	Moderate–High	High	High	Strong	Moderate

(Continued)

Table 10 (continued)

Approach	Data Requirement	Model Complexity	Computational Cost	Physics Integration	Suitability for Early Design
Present work (GPR + low-complexity ANN)	Low–Moderate	Low	Low	Implicit (synthetic equations)	High

The primary objective of this study is to enable efficient early-stage design exploration rather than comprehensive high-fidelity prediction. Therefore, low-complexity surrogate models, including GPR and shallow ANNs, were selected to achieve a balance among accuracy, interpretability, and computational efficiency. GPR inherently provides uncertainty estimates, while the simplified ANN architecture reduces the risk of overfitting when training data are limited.

The proposed framework complements state-of-the-art physics-informed and operator-learning approaches. Future research will explore hybrid extensions that incorporate physics-based constraints or operator-learning concepts, while maintaining the computational efficiency demonstrated in the current study.

The ANSYS FE results have been compared with surrogate predictions to generate global accuracy metrics that assess surrogate quality. This finding confirms the close agreement between the high-fidelity simulations and the surrogate, as shown in Table 11.

Table 11: Global accuracy and uncertainty metrics of surrogate predictions compared with ANSYS simulations.

Metric	Stress	Deflection
Mean absolute error (%)	1.15	1.41
RMSE (%)	1.33	1.63
Error variance	0.45	0.67
Maximum error (%)	2.34	2.59

With a relatively small error variance, surrogate accuracy is stable across the design space, without localized degradation. Based on these global metrics, we can confirm the robustness of the surrogate model for early-stage aerospace TPE design optimization.

The proposed geometry-driven optimization framework complements recent material-focused strategies for improving thermoplastic elastomer (TPE) performance. While previous studies have enhanced the mechanical response of aerospace-grade TPEs, such as TPU and COPE, by modifying molecular architecture and filler content [24], this work focuses on geometric design variables to achieve similar gains without altering material properties. This method offers a parallel and computationally efficient optimization pathway.

The surrogate models in this study achieve prediction errors of approximately 2%, meeting accepted standards for reduced-order predictive models in aerospace structural design and optimization workflows [1]. This level of accuracy supports surrogate-assisted multi-objective optimization as a reliable alternative to direct high-fidelity FEA in early-stage design exploration.

6 Conclusion

An optimization framework for TPE components in aerospace applications is presented based on data-driven surrogate analysis. Through the combination of neural network surrogates with multi-objective genetic algorithms, the authors demonstrate efficient exploration of the design space and efficient production of high-quality Pareto fronts. The primary contribution of this study is to demonstrate that strategic simplification of surrogate-based optimization pipelines, when guided by established methodologies, produces robust and efficient design tools. Rather than introducing new optimization or ML algorithms, this study focuses on methodological simplification and practical deployment. The results demonstrate that carefully configured, low-complexity surrogate models can achieve accuracy comparable to more advanced methods, challenging the prevailing trend toward increasingly complex data-driven frameworks in elastomer optimization. Moreover, the proposed framework is particularly suited for aerospace-grade TPUs and COPEs, where rapid assessment of stiffness–damping–stress trade-offs is essential during early-stage design.

The method can also be extended to more complex problems involving fatigue, viscoelasticity, and multiphysics coupling, providing a scalable and adaptable solution for material-structure design challenges in aerospace. As a result of this research, the following conclusions can be drawn:

1. The NN-GA framework reduced computational cost by ~90% while maintaining <3% error.
2. Optimal design for the studied plate occurs at AR between 0.5–1.0 and TR ≈ 0.2.
3. Parameter sensitivity ranked as: x1 (AR) most influential on deflection, etc.).
4. According to the comparison, the surrogate model demonstrated high accuracy with a mean deviation of 1.18% and a maximum deviation of 2.6%. As a result, computational costs are effectively reduced and reliable performance is maintained. Also, it shows that the surrogate model is capable of generalizing beyond the training data and predicting optimal solutions with good accuracy.

ANSYS produces accurate simulation results for both stress and displacement in most configurations tested. Considering the rare outliers, it may be possible to improve the material or boundary condition modeling, further calibrate, enhance mesh resolution, or refine the calibration of the model. The primary limitation of this study is its reliance on a simple ground-truth function, along with the use of a simplified material model, 2D geometric parameterization, and the lack of dynamic or thermal loading.

Future investigations should incorporate FEM analysis (FEA) or empirical measurement data and expand the training dataset through adaptive or active learning strategies. Incorporating additional design parameters and more complex geometries and boundary conditions would further enhance the applicability of the approach. The surrogate models were trained on a dataset of 50 samples, which is adequate for a proof-of-concept but may compromise stability and robustness in higher-dimensional or more nonlinear design spaces. The use of analytically generated synthetic functions, rather than high-fidelity simulations, facilitated efficient exploration of the design space and reduced computational costs; however, this may limit generalizability to complex real-world scenarios. A more rigorous global sensitivity analysis, such as Sobol variance-based indices, will be considered in future work to better quantify higher-order interactions between design variables. Addressing these limitations is expected to improve predictive robustness and support application to industrial-scale design problems.

Although this study centers on synthetic analytical benchmarks, the observed reduction in computational cost and strong agreement with ANSYS validation support future application of the framework to real multiphysics simulation and experimental datasets. Incorporate real FEA and experimental data to capture fatigue or viscoelastic responses. Expand the design variables to include material composition, such as filler percentage. Additionally, validate the approach with a physical prototype of an aerospace component, for example, a seal or a damper.

Finally, although the current formulation does not address all operational complexities present in aerospace environments, the proposed methodology can be extended. Subsequent research will integrate more realistic geometries, multiphysics constraints, and certification-relevant performance criteria to bridge the gap between early-stage optimization and detailed aerospace design workflows.

Acknowledgement: None.

Funding Statement: The authors received no specific funding for this study.

Author Contributions: The authors confirm contributions to the paper as follows: Conceptualization, Adwaa Abdulmajeedand, Duaa Abdul Rida Musa and Ola Abdul Hussain; methodology, Adwaa Abdulmajeedand, Duaa Abdul Rida Musa and Ola Abdul Hussain; validation, Adwaa Abdulmajeedand, Emad Kadum Njim; formal analysis, Adwaa Abdulmajeedand, Duaa Abdul Rida Musa; investigation, Duaa Abdul Rida Musa and Ola Abdul Hussain; resources, Emad Kadum Njim and Royal Madan; data curation, Adwaa Abdulmajeedand and Duaa Abdul Rida Musa; writing—review and editing, Adwaa Abdulmajeedand, Duaa Abdul Rida Musa, Ola Abdul Hussain, Emad Kadum Njim and Royal Madan; project administration, Emad Kadum Njim and Royal Madan; funding acquisition, Adwaa Abdulmajeedand, Emad Kadum Njim. All authors reviewed and approved the final version of the manuscript.

Availability of Data and Materials: The authors confirm that the data supporting the findings of this study are available within the article.

Ethics Approval: Not applicable.

Conflicts of Interest: The authors declare no conflicts of interest.

References

1. Tserpes K, Sioutis I. Advances in composite materials for space applications: a comprehensive literature review. Aerospace. 2025;12(3):215. doi:10.3390/aerospace12030215.
2. Abbas EN, Abud Ali ZAA, Njim EK, Flayyih MA, Madan R. Analytical and numerical investigation of free vibration of nanoparticle-reinforced composite cylindrical shells. Diagnostyka. 2025;26(1):201249. doi:10.29354/diag/201249.
3. Alhous ZFA, Jweeg MJ, Njim EK, Mouthanna A, Flayyih MA, Madan R, et al. Nonlinear frequency and dynamic response of PLA polymeric imperfect FG sandwich plates under hygrothermal conditions. Coupled Syst Mech. 2025;14:1–19.
4. Ozturk F, Cobanoglu M, Ece RE. Recent advancements in thermoplastic composite materials in aerospace industry. J Thermoplast Compos Mater. 2024;37(9):3084–116. doi:10.1177/08927057231222820.
5. Sahu BB, Moharana S, Behera PK. Elastomeric-based composite materials for engineering applications. In: Polymer composites. Singapore: Springer Nature; 2024. p. 329–55. doi:10.1007/978-981-97-2075-0_11.
6. Ghoreishy MHR, Razavi-Nouri M, Naderi G. Finite element analysis of flow of thermoplastic elastomer melt through axisymmetric die with slip boundary condition. Plast Rubber Compos. 2000;29(5):224–8. doi:10.1179/146580100101540996.
7. Ghoreishy MHR, Razavi-Nouri M, Naderi G. Finite element analysis of a thermoplastic elastomer melt flow in the metering region of a single screw extruder. Comput Mater Sci. 2005;34(4):389–96. doi:10.1016/j.commatsci.2005.01.011.
8. Chen D, Miao Y, Xu D, Li S, Li T, Peng C, et al. Micro cross-linking strategy with dynamic covalent bond for high-performance epoxy-based thermoplastic polymer and polymer composites. Compos Part A Appl Sci Manuf. 2026;200:109324. doi:10.1016/j.compositesa.2025.109324.
9. Kadum Njim E, Ziadoon Mohammed Rahi AH, Jweeg MJ, Sameer Jabbar M, Al-Maamori MH, Madan R. Dynamic analysis of composite plates reinforced with MWCNT nanoparticles: theoretical and experimental study. Aircr Eng Aerosp Technol. 2026;98(1):1–11. doi:10.1108/aeat-08-2024-0224.

10. Sadeghzade M, Dadashi A, Gharehbaghi H. Mechanical behavior, process innovations, and future directions of 3d-printed continuous fiber-reinforced polymeric lattice structures: a comprehensive review. Mater Des. 2025;260:114970. doi:10.1016/j.matdes.2025.114970.
11. Wang Y, Wang K, Zhang C. Applications of artificial intelligence/machine learning to high-performance composites. Compos Part B Eng. 2024;285:111740. doi:10.1016/j.compositesb.2024.111740.
12. Dong Y, Chen Z, Zhao Y. Hybrid genetic algorithm with interpretable surrogate modeling for enhanced optimization of short-fiber reinforced polymer composites. Mater Des. 2025;258:114611. doi:10.1016/j.matdes.2025.114611.
13. Azimi M, Foran G, Barcha C, St-Antoine C, Prébé A, Dollé M. Optimizing the dry processing parameters of thermoplastic vulcanizate electrolytes for improved microstructure and its impact on electrochemical stability. Mater Adv. 2025;6(12):3945–56. doi:10.1039/d5ma00080g.
14. Restrepo-Zapata NC, Olaya-Munoz DA, Osswald TA, Hernandez-Ortiz JP. Optimizing elastomeric foam extrusion with a chemo-rheologically informed multi-scale computational approach. Mech Mater. 2025;210:105453. doi:10.1016/j.mechmat.2025.105453.
15. Triganza T, Refalo P, Rochman A, Brancaleone RP. Process parameter optimization for sustainable manufacturing of elastomeric components used in water treatment systems. Procedia CIRP. 2025;135:991–6. doi:10.1016/j.procir.2025.01.092.
16. Tao C, Liu C, Wang Y, Yang B. Meta-learning innovates chemical kinetics: an efficient approach for surrogate model construction. Proc Combust Inst. 2025;41:105860. doi:10.1016/j.proci.2025.105860.
17. Moghimi Esfand-Abadi MH, Djavareshkian MH, Madani A. Kriging and radial basis function models for optimized design of UAV wing fences to reduce rolling moment. Int J Intell Syst. 2024;2024:4108121. doi:10.1155/2024/4108121.
18. Singh M, Dhiman S, Singh H, Berndt CC. Optimization of modulation-assisted drilling of Ti-6Al-4V aerospace alloy via response surface method. Mater Manuf Process. 2020;35(12):1313–29. doi:10.1080/10426914.2020.1772487.
19. Stewart P, Fleming PJ, MacKenzie SA. On the response surface methodology and designed experiments for computationally intensive distributed aerospace simulations. In: Proceedings of the Winter Simulation Conference; 2002 Dec 8–11; San Diego, CA, USA. p. 476–82.
20. Yan Q, Wan Z, Yang C. Flight load calculation using neural network residual kriging. Aerospace. 2023;10(7):599. doi:10.3390/aerospace10070599.
21. Kim S, Kim J. Meta pseudo label tabular-related regression model for surrogate modeling. Expert Syst Appl. 2025;261:125520. doi:10.1016/j.eswa.2024.125520.
22. Samadian D, Muhit IB, Occhipinti A, Dawood N. Meta databases of steel frame buildings for surrogate modelling and machine learning-based feature importance analysis. Resilient Cities Struct. 2024;3(1):20–43. doi:10.1016/j.rcns.2023.12.001.
23. Zhu YP, Liu Z, Cheng L, Lang Z. Data-driven science and physically interpretable machine learning for complex dynamic systems. In: Encyclopedia of systems and control engineering. Amsterdam, The Netherlands: Elsevier; 2026. p. 535–52. doi:10.1016/b978-0-443-14081-5.00127-6.
24. Ulkir O, Ersoy S. Hybrid experimental-machine learning study on the mechanical behavior of polymer composite structures fabricated via FDM. Polymers. 2025;17(15):2012. doi:10.3390/polym17152012.